Journal of Fluids and Structures (1999) **13,** 935–954
Article No.: jfls. 1999.0237, available online at http://www.idealibrary.com on IDEAL®

FREE SURFACE WAVE INTERACTION WITH A HORIZONTAL CYLINDER

P. Oshkai and D. Rockwell

Department of Mechanical Engineering and Mechanics, 354 Packard Laboratory, 19 Memorial Drive West, Lehigh University, Bethlehem, PA 18015, U.S.A.

(Received 15 October 1998 and in revised form 6 April 1999)

Classes of vortex formation from a horizontal cylinder adjacent to an undulating free-surface wave are characterized using high-image-density particle image velocimetry. Instantaneous representations of the velocity field, streamline topology and vorticity patterns yield insight into the origin of unsteady loading of the cylinder. For sufficiently deep submergence of the cylinder, the orbital nature of the wave motion results in multiple sites of vortex development, i.e., onset of vorticity concentrations, along the surface of the cylinder, followed by distinctive types of shedding from the cylinder. All of these concentrations of vorticity then exhibit orbital motion about the cylinder. Their contributions to the instantaneous values of the force coefficients are assessed by calculating moments of vorticity. It is shown that large contributions to the moments and their rate of change with time can occur for those vorticity concentrations having relatively small amplitude orbital trajectories. In a limiting case, collision with the surface of the cylinder can occur. Such vortex–cylinder interactions exhibit abrupt changes in the streamline topology during the wave cycle, including abrupt switching of the location of saddle points in the wave. The effect of nominal depth of submergence of the cylinder is characterized in terms of the time history of patterns of vorticity generated from the cylinder and the free surface. Generally speaking, generic types of vorticity concentrations are formed from the cylinder during the cycle of the wave motion for all values of submergence. The proximity of the free surface, however, can exert a remarkable influence on the initial formation, the eventual strength, and the subsequent motion of concentrations of vorticity. For sufficiently shallow submergence, large-scale vortex formation from the upper surface of the cylinder is inhibited and, in contrast, that from the lower surface of the cylinder is intensified. Moreover, decreasing the depth of submergence retards the orbital migration of previously shed concentrations of vorticity about the cylinder.

1. INTRODUCTION

The interaction of waves with structures in the ocean environment is a major source of unsteady loading and vibration of a variety of structural components including long cables, components of offshore platforms, risers, as well as a number of other related geometrical configurations. In recent decades, substantial efforts have been devoted to enhancing our understanding of this class of flow-structure interaction. In the present investigation, the focus is on wave interaction with a horizontal cylinder. Previous related studies may be categorized according to a circular cylinder in oscillatory flow, a cylinder in orbital flow/orbital motion, and a cylinder beneath a nominally stationary free surface. Summaries of these efforts are provided in the following.

1.1. Circular Cylinder in Oscillatory Flow

A variety of theoretical, numerical and experimental investigations have addressed the case of unidirectional, oscillatory flow past a circular cylinder. Sarpkaya and Isaacson (1981)

0889–9746/99/100935 + 20 $30.00

summarize early studies, extending over a range of Keulegan–Carpenter number KC, where $KC = UT/D = 2\pi A/D$, in which U is the maximum velocity of the flow, T is the period of the wave motion, D is the cylinder diameter, and A is amplitude. Recent investigations include those of Singh (1979), Honji (1981), Bearman *et al.* (1981), Sarpkaya & Isaacson (1981), Ikeda & Yamamoto (1981), Iwagaki *et al.* (1983), Williamson (1985), Sarpkaya (1986), Obasaju *et al.* (1988), and Tatsuno & Bearman (1990). These investigations provide insight into, among other features, the vortex patterns that can arise over various ranges of KC.

From a theoretical perspective, description of the relationship between point vortices and loading on a cylinder was formulated by Sarpkaya (1963, 1968, 1969). Using this type of approach, Maull & Milliner (1978) qualitatively related the movement of visualized vortices about the cylinder to variations of the measured forces. Ikeda & Yamamoto (1981) approximated the variation of the lift force by tracking vortices and estimating their circulation using particle streak-marker visualization. Lin & Rockwell (1996) employed quantitative images of the patterns of distributed vorticity generated by an oscillating cylinder, and the lift force was approximated using the Maull-Milliner (1978) approach, whereby each vortex was represented as an equivalent point vortex of given circulation. In addition, the vorticity moment approach of Lighthill (1986) was employed to account for the distributed nature of the instantaneous patterns of vorticity. Noca *et al.* (1997) extended this technique to account for vorticity outside the field of view of the near wake of the cylinder. Unal *et al.* (1997) and Noca (1997) invoked yet another class of approaches for evaluating the forces. These methods, which are based on instantaneous patterns of velocity obtained by quantitative imaging, involve momentum-based approaches that employ a control volume about the cylinder.

Numerical approaches to this class of flows include a variety of techniques. Discrete vortex methods have been employed and are reviewed by Sarpkaya (1989) and Lin *et al.* (1996). Finite-difference solutions of the Navier–Stokes equations were used by Baba & Miyata (1987), Wang & Dalton (1991), Justesen (1991) and Miyata & Lee (1990). Solution of the Navier–Stokes equations has also been approached by Anagnostopoulos *et al.* (1995) using a finite-element analysis and by Sun & Dalton (1996) via a method of large eddy simulation.

Insight into the decomposition of forces on cylinders in small-amplitude oscillatory flows is provided by Bearman *et al.* (1985a). The total force was considered to be composed of three parts: inertia of the accelerating flow; effects of viscous boundary layers, and shedding of vortices. Since this investigation focused on low values of KC, the dominant part of the force is the inviscid inertia force. Onset of vortex shedding from a circular cylinder and a substantial contribution to the force occurs at a value of KC of the order of 5.

The rich variety of vortex patterns that are generated at larger values of flow (or cylinder) oscillation amplitude, i.e., $KC = 2\pi A/D$, are summarized, for example, by Sarpkaya & Isaacson (1981), Williamson (1985) and Obasaju *et al.* (1988). The interrelationship between vortex patterns and the induced forces on the cylinder were addressed by Obasaju *et al.* (1988) for values of KC up to 55. Over this range, the patterns of vortex formation were classified as asymmetric, transverse, diagonal and quasi-steady, which, in turn, have important consequences for the forces on the cylinder. Lin & Rockwell (1999) employed a technique of high-image-density particle image velocimetry to determine the instantaneous patterns of vorticity and velocity about the cylinder at a value of $KC = 10$. The physics of vortex formation were shown to involve a complex series of events, described by vorticity and streamline topology. Moreover, in the presence of a free surface, the nature of vortex formation was found to be a strong function of the degree of submergence of the cylinder. These features were related to signatures of instantaneous lift.

1.2. Circular Cylinder in Orbital Flow/Orbital Motion

In the event that orbital, as opposed to unidirectional, flow interacts with the cylinder, or equivalently, orbital versus unidirectional motion of the cylinder occurs in quiescent fluid, the processes of vortex formation and the associated loading are expected to be altered accordingly. Due to the orbital particle trajectories inherent to a wave, the velocity vectors of the water particles rotate, in contrast to the horizontally directed velocities of a unidirectional, oscillatory flow. This distinction was emphasized by Ramberg & Niedzwecki (1979), who addressed the differences of the inertia C_m and drag C_d coefficients of Morison's equation for planar oscillatory flow versus orbital flow.

Chaplin (1981a) calculated the limiting case of irrotational flow around a horizontal cylinder under long-crested waves, using Milne–Thompson's circle theorem. The presence of the cylinder was found to significantly distort the wave flow. Fully accounting for viscous effects, Borthwick (1986) performed a finite-difference solution of the Navier–Stokes equations for the case of flow due to orbital motion of a cylinder. Further numerical studies involving orbital wave motion past a circular cylinder were performed by Miyata & Lee (1990) and Chaplin (1992, 1993). These studies show the substantial influence of viscous effects and, at sufficiently high values of KC, the possibility of vortex formation, which significantly influences the flow patterns and the corresponding forces on cylinders in wave-induced flows.

Corresponding experimental investigations have focused primarily on measurement of the loading on a cylinder. The forces on bodies in orbital motion were measured by Holmes & Chaplin (1978), Chaplin (1981b), Sarpkaya (1984), Grass *et al.* (1985), Borthwick (1987), and Chaplin (1988). Williamson *et al.* (1998) characterized the fluid loading and vortex dynamics for a cylinder moving in elliptic orbits. It was found that as the ellipticity of the orbit increases, there is a significant reduction in the drag force. Moreover, for circular orbits, the mean radial force is directed inwards relative to the orbit, due to the background circulation set up by repeated orbital cycles for the case of orbital wave motion past a stationary cylinder. For the case of wave motion past a stationary cylinder, Chaplin (1984) determined the forces on the cylinder for relatively low $\mathrm{KC} < 3$. For $\mathrm{KC} < 2$, the inertial force provides the dominant contribution to the loading. For $\mathrm{KC} > 2$, nonlinear contributions to the loading were found to be substantial. Forces on horizontal cylinders under periodic and random waves, at Keulegan–Carpenter numbers up to 20, were measured by Bearman *et al.* (1985b). The force coefficients were found to be similar for regular and random waves. In random waves, the vortex shedding is triggered when KC exceeds a value of 7.

1.3. Circular Cylinder beneath a nominally Stationary Free Surface

In contrast to the foregoing cases of oscillatory or orbital flow, or the corresponding motion of a cylinder in quiescent fluid, where the presence of the free surface has not been an issue, recent investigations have addressed the consequence of proximity of a free surface on the patterns of vortices formed both from the cylinder and the free surface.

Miyata *et al.* (1990) studied the steady translation of a cylinder beneath a free surface via qualitative visualization and numerical simulation. Using particle streaks and focussing on the case where the free surface exhibited negligible distortion, they show interesting patterns of vortices, which were interpreted with corresponding force measurements. Sheridan *et al.* (1997) undertook a quantitative investigation of the nominally steady flow past a cylinder close to a free surface, using the technique of high-image-density particle image velocimetry. The value of Froude number was sufficiently high, such that substantial distortion of the

free surface could occur. Patterns of instantaneous velocity and vorticity exhibit a variety of fundamental mechanisms of generation of vorticity layers from the cylinder and the free surface. The development and interaction of these layers suggest important consequences for the loading of the cylinder. In the event that a cylinder penetrates the free surface and is subjected to oscillation in the vertical direction, while the Froude number is maintained sufficiently low to avoid significant free-surface distortions, still additional classes of vorticity concentrations can develop in the near-wake of the cylinder, as characterized by Lin *et al.* (1996). The foregoing features may be present, in analogous forms, for wave motion past a cylinder located close to a free surface; this aspect has remained, however, uninvestigated.

1.4. Unresolved Issues

The foregoing studies have provided considerable insight into the flow patterns and loading due to oscillatory or orbital flow past a cylinder, or the equivalent motion of a cylinder in quiescent fluid. To date, an experimentally based investigation that provides representations of the instantaneous, quantitative flow patterns about the cylinder, acquired simultaneously with the measured loading, has not been undertaken. At a sufficiently high value of Keulegan–Carpenter number KC, it is well known that shedding of vortices will occur, but the manner in which these vortices are initially formed and shed from the cylinder has not been addressed. Moreover, the nature of their orbital migration about the cylinder is unclear. An intriguing possibility is the formation of vortices from multiple sites about the surface of the cylinder during the imposed orbital motion of the wave cycle, in contrast to what is known for the case of unidirectional oscillatory flow or, for that matter, for the well-known case of Kármán vortex formation from a cylinder in a uniform stream. Moreover, the eventual shedding of a number of vortices from the cylinder during an orbital cycle of the wave motion is expected to produce patterns of multiple, interacting vortices; the issue of whether the trajectories of these vortices follow closely the imposed orbital motion of the wave, or are primarily influenced by mutual induction effects, has not been characterized. An adequate understanding of all of these complex features requires space–time characterization of the instantaneous patterns of vorticity and streamline topology, in conjunction with instantaneous force measurements. The present investigation employs this approach.

2. EXPERIMENTAL SYSTEM AND TECHNIQUES

2.1. Wave Tank

Waves were generated with a paddle-type wavemaker having actively controlled force feedback to compensate for wave reflections. The total height of the wavemaker was 0·90 m, relative to the depth 0·75 m of the quiescent water. At the opposite end of the wave tank of length 9 m, a wedge-type beach constructed of absorbent foam material provided additional attenuation of reflected waves. The motivation of the present investigation is the particularly severe loading of structures occurring in a system of incident-reflected wave systems having orbital particle trajectories of the type defined in the visualization of Van Dyke (1982).

The limiting case is a pure standing wave; such wave–cylinder interactions are described for a number of practical scenarios by Naudascher & Rockwell (1994). A major criterion of the present experiments was to retain the orbital character of the local wave motion past the cylinder, while attaining essentially phase-locked, spanwise coherent vortex formation. Preliminary experiments revealed that wave motion having circular orbits, i.e., particle

trajectories, yielded degeneration of phase-repetitive vortex shedding and intermittent loss of quasi-dimensionality of the shed vortices, relative to waves having at least 2 : 1 elliptical orbits. These considerations led to the generation of an orbital particle trajectory of the wave motion by adjustment of the beach. The orbital trajectory had the following characteristics: ratio of major to minor axis of 3 : 1; angle of inclination θ of approximately 41° with respect to the horizontal; and ratio of major axis to the cylinder diameter of 2·2 : 1, corresponding to an effective Keulegan–Carpenter number KC = 6·96 based on the amplitude of the major axis. These parameters were determined at a location 2·35D to the left of the center of the cylinder, and at a constant depth of 1·57D beneath the quiescent free surface. At this reference location, a total of 225 instantaneous velocity vectors were spatially averaged over a square domain $0{\cdot}97D \times 0{\cdot}97D$, in order to obtain a single, representative instantaneous vector of the wave motion. The maximum vector magnitudes of the wave motion, $|V|$, occurred in the first quadrant ($\theta = 44°$, $|V| = 0{\cdot}044$ m/s) at instants corresponding to image frame numbers (defined subsequently) $N = 4$ and 20, and in the third quadrant ($\theta = 224°$, $|V| = 0{\cdot}034$ m/s) at $N = 11$. At the deepest value of submergence, $h/D = 1{\cdot}57$, distortion of the wave motion at the reference location due to the presence of the cylinder is minimal, except for that portion of the wave cycle for which the vorticity moves towards the reference location. At shallower depths of submergence, especially for the surface piercing case, $h/D = 0$, significant distortions of the wave system occur in the near field of the cylinder, i.e., at the reference location.

2.2. Experimental Apparatus

A horizontal cylinder extending along the entire width of the wave tank was located a distance of approximately 7·7 m from the wave paddle. The support system allowed adjustment of the vertical position of the cylinder to various depths of submergence h, as defined in Figure 1. The cylinder had a diameter $D = 1{\cdot}27$ cm and a length of 36·8 cm. It was mounted on a 3.2 mm^2 sting with an arrangement of eight strain gauges to measure the in-line and transverse components of the fluid loading. End-plates were employed at either end of the cylinder. The end-plate was 3 mm-thick Plexiglas, which allowed use of particle image velocimetry. The gap between the end of the cylinder and this end-plate was kept at 0·7 mm. On the far side of the cylinder, the end-plate had a thickness of 6·4 mm; it was beveled at an angle of 30°. This end-plate was mounted in such a fashion that it did not come in contact with the cylinder or the support sting. In order to allow penetration of the sheet of laser light through the cylinder with minimum refraction, a 12 mm-wide thin-wall window was machined in the cylinder. The center of this window was located a distance of 12 mm from the end of the cylinder, which was within the region of spanwise coherent vortex formation, as visualized with a scanning laser sheet across the tank. The window was filled with distilled water. The entire cylinder–end-plate system could be subjected to controlled motion in either the horizontal or vertical direction using computer-controlled motion. For purposes of the present study, this motion was employed only to calibrate the strain gauge system.

Known in-line and transverse forces are required for suitable calibration of the strain gauge sting. The cylinder was oscillated at the Keulegan–Carpenter numbers of 1 and 10, and the r.m.s. of the force coefficient $C_{F\mathrm{rms}}$ was measured for both in-line and transverse motions of the cylinder, then compared with the results of Bearman *et al.* (1985). Herein, instantaneous force coefficients C_x and C_y are employed. They are defined as $C_x = F_x/[\frac{1}{2}\rho U^2 Dl]$ and $C_y = F_y/[\frac{1}{2}\rho U^2 Dl]$, where F_x and F_y are the horizontal and vertical dimensional forces, ρ is the fluid density, U is the maximum velocity of the orbital motion of the wave, and D and l are the cylinder diameter and length respectively. Positive F_y

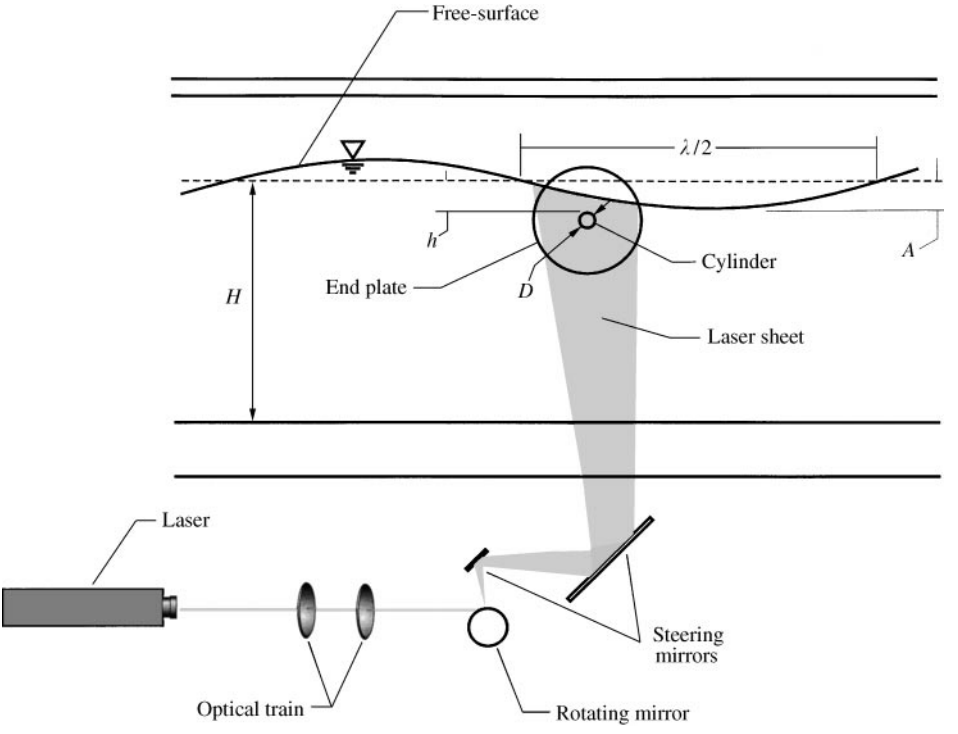

Figure 1. Overview of experimental arrangement and principal parameters for interaction of a progressive wave with the cylinder.

corresponds to an upward force on the cylinder, and positive F_x is the force on the cylinder in the direction of wave propagation (from left to right).

2.3. Image Acquisition and Processing

Quantitative images of the wave–cylinder interaction were obtained using a laser-scanning version of high-image-density particle image velocimetry (PIV). The laser scanning approach is described in detail by Rockwell *et al.* (1993). Laser illumination is provided by a continuous–wave argon-ion laser having a maximum power of 30 W and operating in the multi-line mode. The output from the laser passes through a series of optical lenses which focus the beam at approximately the vertical elevation of the cylinder in the wave tank. This beam is then focused on a 72-faceted rotating mirror. For the present experiments, the mirror was driven at a rotation rate corresponding to an effective scanning frequency of 208·8 Hz. This approach generated multiply-exposed particle images by illumination of metallic-coated glass particles having an average diameter of 14 μm. This entire system of the focusing optics and rotating mirror were positioned on an optical table that could be rotated and translated located beneath the wave tank.

Images were recorded with a 35 mm camera operating at a framing rate of approximately 8 frames/s, which corresponded approximately to 16 frames during one cycle of the wave motion, which had a period T of 2 s. The temporal resolution of the cinema acquisition of images was therefore $\Delta t/T = 0{\cdot}0625$. The 35 mm film had a resolution of 300 lines/mm. In order to preclude directional ambiguity, a rotating bias mirror was employed in front of the 100 mm telephoto lens of the 35 mm camera. Systematic errors associated with mirror

rotation were avoided by maintaining the angular displacement of the mirror during the shutter opening at a value much less than 1°.

The 35 mm photo negative was scanned at a resolution of 125 pixels/mm. A single-frame cross-correlation method, involving the application of two successive fast Fourier transforms, was employed to provide the velocity vector over the interrogation window, which had a size of 90×90 pixels ($0{\cdot}72$ mm $\times$ $0{\cdot}72$ mm), corresponding to a grid size of $0{\cdot}36$ mm $\times$ $0{\cdot}36$ mm on the film. In order to satisfy the high-image-density criterion, each interrogation window contained a minimum of 50 multiply-exposed particle images. The velocity field was smoothed using a Gaussian-weighted average technique described by Landreth & Adrian (1989), with the smoothing parameter $p = 1{\cdot}3$, which provides minimal distortion of the velocity field.

3. WAVE INTERACTION WITH A WELL-SUBMERGED CYLINDER: PATTERNS OF VORTICITY AND VELOCITY-STREAMLINE TOPOLOGY

Figures 2(a) and 2(b) show the time evolution of patterns of vorticity. In addition, Figure 2(a) exhibits corresponding patterns of instantaneous velocity and superposed streamlines, and Figure 2(b) gives close-ups of the patterns of velocity vectors near key vorticity concentrations. Contours of positive and negative vorticity are designated respectively by solid and dashed lines. The time sequence of images is represented by excerpts from the sequence of frames $N = 7$ through 19, which extend over nearly one complete cycle of the wave motion. At the instants corresponding approximately to frames $N = 7$ and 15, the free surface attains its maximum and minimum elevations, respectively.

Frame $N = 7$ shows three major concentrations of vorticity. Negative vortex A is shed from the top of the cylinder, while positive vortices B and D develop respectively along the right and bottom sides of the cylinder. Positive vortex C was generated during the previous cycle of the wave motion and is located above the cylinder. The corresponding image of the velocity field at $N = 7$ shows that the instantaneous direction of the wave is essentially from left to right, i.e., the velocity vectors in the region of the undistorted wave away from the cylinder are horizontal and essentially parallel to the free surface. The locus of vortex A is clearly identifiable in the instantaneous streamline pattern, which takes the form of a limit cycle. A saddle point (locus of intersecting streamlines) is located immediately to the right of this limit cycle. Moreover, an alleyway flow occurs in the region between the right half of the cylinder and the streamline that leads to the saddle point. A localized separation bubble is discernible along the right surface of the cylinder; it corresponds to the vorticity concentration B along that surface.

At a later instant, corresponding to frame $N = 9$, further development of vortices A through D is indicated. Vortex A has approximately attained its maximum displacement from the surface of the cylinder, vortices B and D have moved clockwise around the cylinder and vortex C has translated horizontally to the right. At this instant, the velocity field of the undisturbed portion of the wave is oriented in the downward, nearly vertical direction. The large-scale negative vortex A is again clearly defined by the pattern of streamlines. It exhibits an outward-spiral from its center, corresponding to an unstable focus. In contrast to the streamline topology at $N = 7$, the saddle point has now switched to the left side of vortex A. An alleyway flow exists between the top surface of the cylinder and the streamline connected to the saddle point. This alleyway flow is oriented in the leftward direction, which is compatible with the outward-spiraling motion of the velocity field and streamline pattern associated with vortex A.

At the instant corresponding to the frame $N = 11$, vortex A has moved back towards the cylinder and is about to collide with its surface and undergo severe distention. The vorticity

concentration B indicated in frame $N = 9$ has further moved in the clockwise direction about the cylinder, separated from its surface and joined with the vorticity concentration D immediately adjacent to the left side of the cylinder. The consequence is formation of a new, two-part vorticity concentration, henceforth designated as B,D. Vortex C has moved still further to the right, and its peak vorticity level has decreased. The corresponding velocity-streamline pattern indicates that the direction of the undisturbed portion of the wave motion is downward to the left. The identities of vortex A and all remaining concentrations of vorticity are not indicated by the streamline topology.

Further development of the pattern of vorticity at frame $N = 13$ (not shown herein) involves interaction of vortex A with the cylinder and its severe distension about the cylinder surface. At a substantially later instant of time, represented by frame $N = 15$ (top of Figure 2(b), a remnant of vortex A is evident, but the most predominant features are the large-scale vortex B,D that has separated from the surface of the cylinder and, simultaneously, onset of a vorticity concentration A′ immediately adjacent to the left side of the cylinder. Vortex C has continued its orbital-like motion about the cylinder and translated downward relative to its position in frame $N = 11$. At this instant, $N = 15$, the free surface attains its minimum elevation corresponding to the trough of the free surface wave. The corresponding image of the velocity pattern shows an enlarged view of the jet-like flow between the counterrotating vortex system B,D and A′.

In frame $N = 17$, the large-scale positive vortex B,D has translated up and to the left of the cylinder. Vortex A′ has continued to increase in scale while continuing to move in the clockwise direction about the surface of the cylinder and vortex C exhibits a further decrease in maximum vorticity level. The corresponding image of the velocity field again focuses on the jet-like flow associated with the system B,D and A′.

Finally, frame $N = 19$ shows the continued upward movement of vorticity concentration B, along with the matured development of vortex A′, which has migrated further in the clockwise direction about the surface of the cylinder. Furthermore, a new positive vorticity concentration B′ develops along the lower right surface of the cylinder. The zoomed-in view of the velocity field reveals the large velocity gradient associated with the development of vortex A′ in the near wake of the cylinder. This region of high gradient is coincident with the extremum of vorticity concentration A′.

The trajectories of the major vorticity concentrations are shown on the xy plane in Figure 3. These diagrams were obtained from the entire succession of PIV images over approximately one cycle of the wave motion. The position of each vorticity concentration was determined by locating the coordinates of the maximum absolute value of vorticity. This extremum is not necessarily coincident with the centroid; moreover, the shape of the vorticity concentration distorts with time. As a consequence, the trajectories of Figure 3 must be viewed as approximate. Nevertheless, the generally orbital trajectories of positive vorticity concentrations are evident in the left diagram and negative concentrations in the right diagram. The direction of the vortex motion is indicated by the arrows.

Since the flow pattern was generally repeatable from cycle to cycle, the paths of positive vorticity concentrations B′, B and E shown in the left diagram essentially represent the continuous trajectory of the vorticity concentration that is initially formed along the right side of the cylinder, moves along the cylinder surface, is shed from the bottom of the cylinder surface, and follows its orbit about the cylinder. Likewise, concentrations D and C represent the trajectory of the concentration that is originally formed along, then shed from the left side of the cylinder. Finally, the paths of the negative concentrations of vorticity A and A′ given in the right diagram represent the trajectory of the concentration that is formed along the left side of the cylinder, moves along the cylinder surface, then eventually separates from the upper surface of the cylinder; its small orbital trajectory leads to eventual collision with

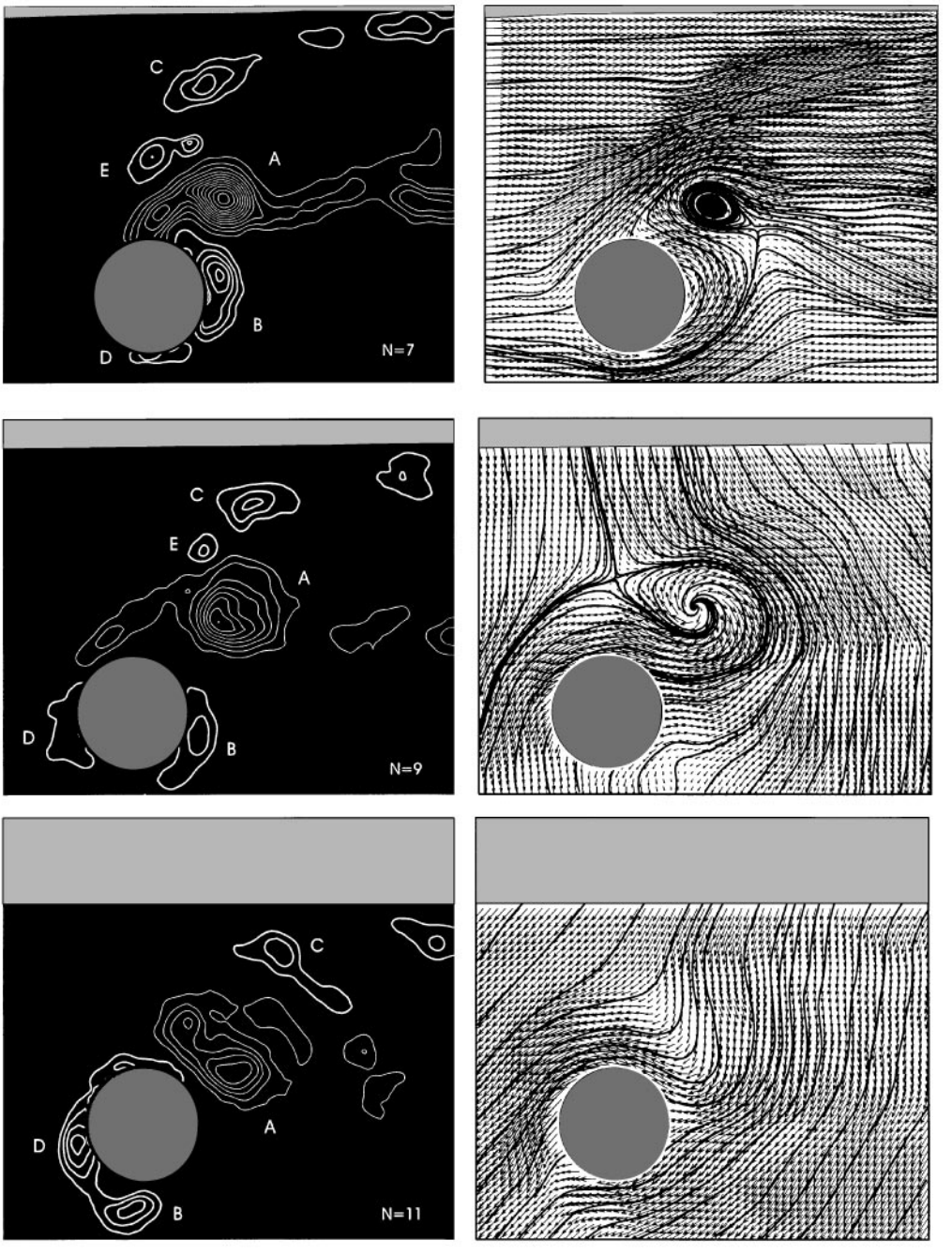

Figure 2(a). Time history of patterns of positive (thick line) and negative (thin line) concentrations of vorticity and corresponding velocity field and streamline topology for the case of relatively deep submergence of the horizontal cylinder beneath the free surface wave. Frame number of cinema sequence is designated by N. Nominal submergence of the cylinder is $h/D = 1{\cdot}57$. Minimum and incremental values of vorticity are $\omega_{\min} = \Delta\omega = 3\ \mathrm{s}^{-1}$.

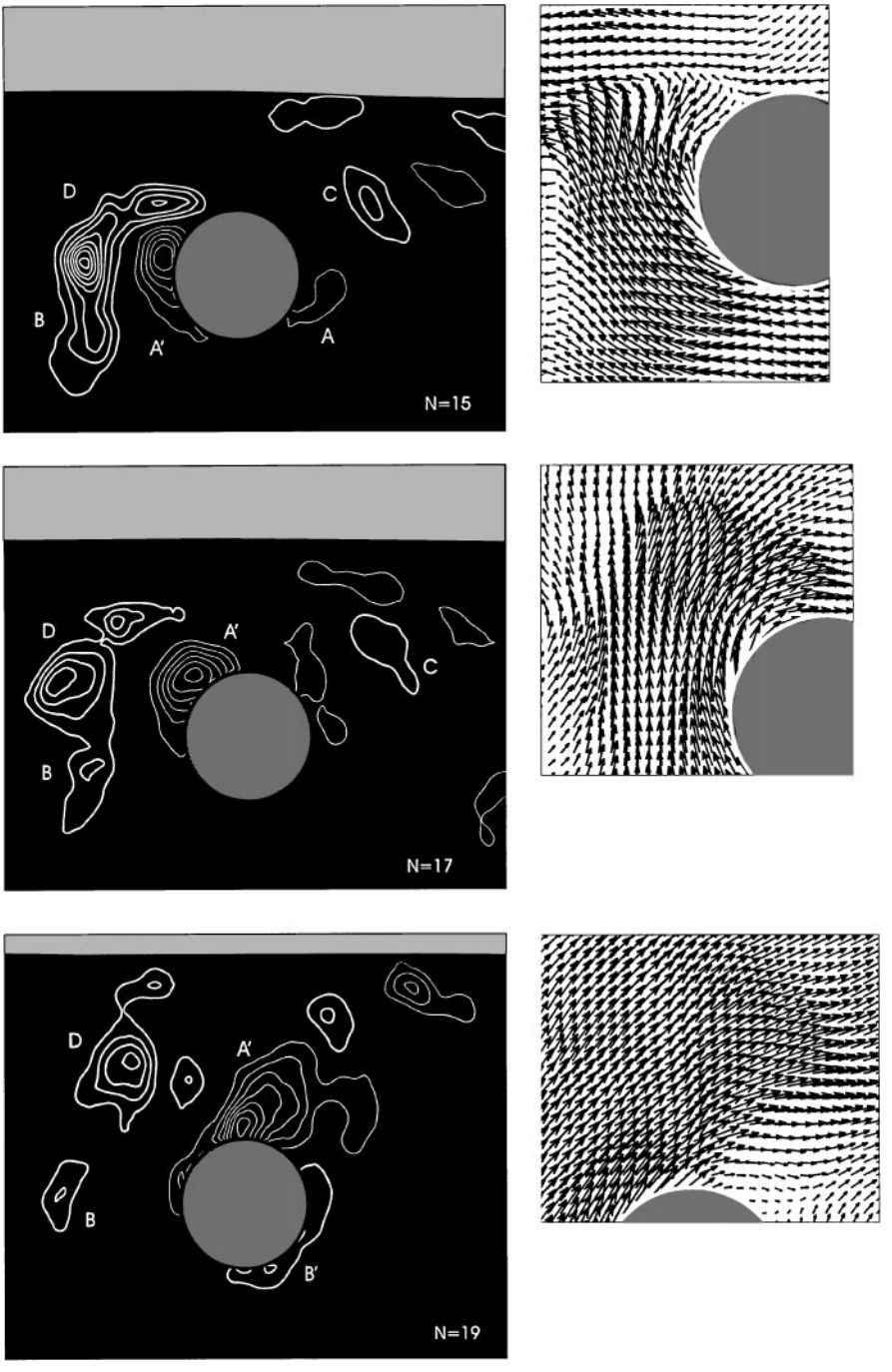

Figure 2(b). Time history of patterns of positive (thick line) and negative (thin line) concentrations of vorticity and zoomed-in representations of corresponding velocity fields associated with vortex pairs for the case of relatively deep submergence of the horizontal cylinder beneath the free surface wave. Frame number of cinema sequence is designated by N. Nominal submergence of the cylinder is $h/D = 1{\cdot}57$. Minimum and incremental values of vorticity are $\omega_{\min} = \Delta\omega = 3\ \mathrm{s}^{-1}$.

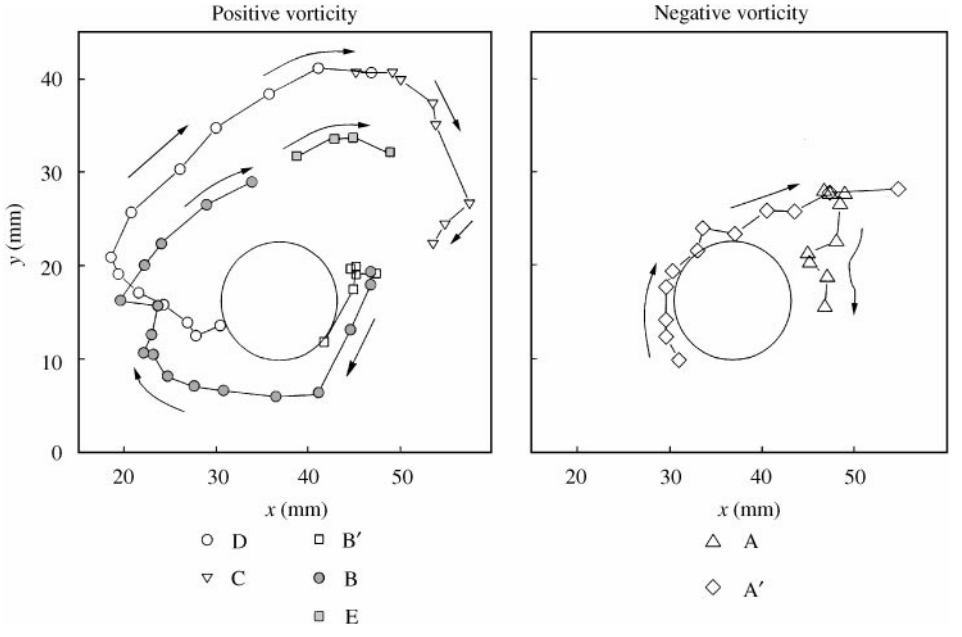

Figure 3. Illustration of the principal types of trajectories of the separated vorticity concentrations due to positive and negative vorticity concentrations. Level of submergence of cylinder beneath the free surface is $h/D = 1{\cdot}57$.

the surface of the cylinder. Viewing all of the foregoing processes together, it is evident that, during a single cycle of the wave motion, vortex formation originates at three distinct sites, followed by eventual shedding from three locations along the surface of the cylinder, i.e. approximately on the upper, lower, and left surfaces.

The orbits of the positive vorticity concentrations shown in the left diagram of Figure 3 have ratios of major to minor axes of roughly 1·6 : 1 and 1·5 : 1 and are inclined at an angle of about 36° to the horizontal. These values compare with those of the wave orbit in the vicinity of the cylinder of 2·2 : 1 and 41°. No doubt, mutual induction and image effects influence the paths of the vortical structures. Yet the reasonable correspondence between the wave and vortex orbits suggests that the wave motion exerts a predominant influence.

4. RELATION OF INSTANTANEOUS LOADING OF CYLINDER TO PATTERNS OF VORTICITY

The time histories of the instantaneous horizontal F_x and vertical F_y forces were acquired simultaneously with the instantaneous images of the flow patterns described in the previous section. The force coefficients C_x and C_y are shown in Figure 4 as a function of frame number N and the corresponding elapsed time t; these coefficients are defined in Section 2.2. Patterns of instantaneous vorticity, taken from the sequence of images described in the previous section, are related to the occurrence of minima and maxima of the force coefficients C_x and C_y in Figure 4.

The maximum-negative value of C_x occurs in the vicinity of $N = 12$. At this instant, the large-scale negative vortex A is on the return portion of its trajectory towards the cylinder and is undergoing initial stages of severe distortion during its interaction with the cylinder.

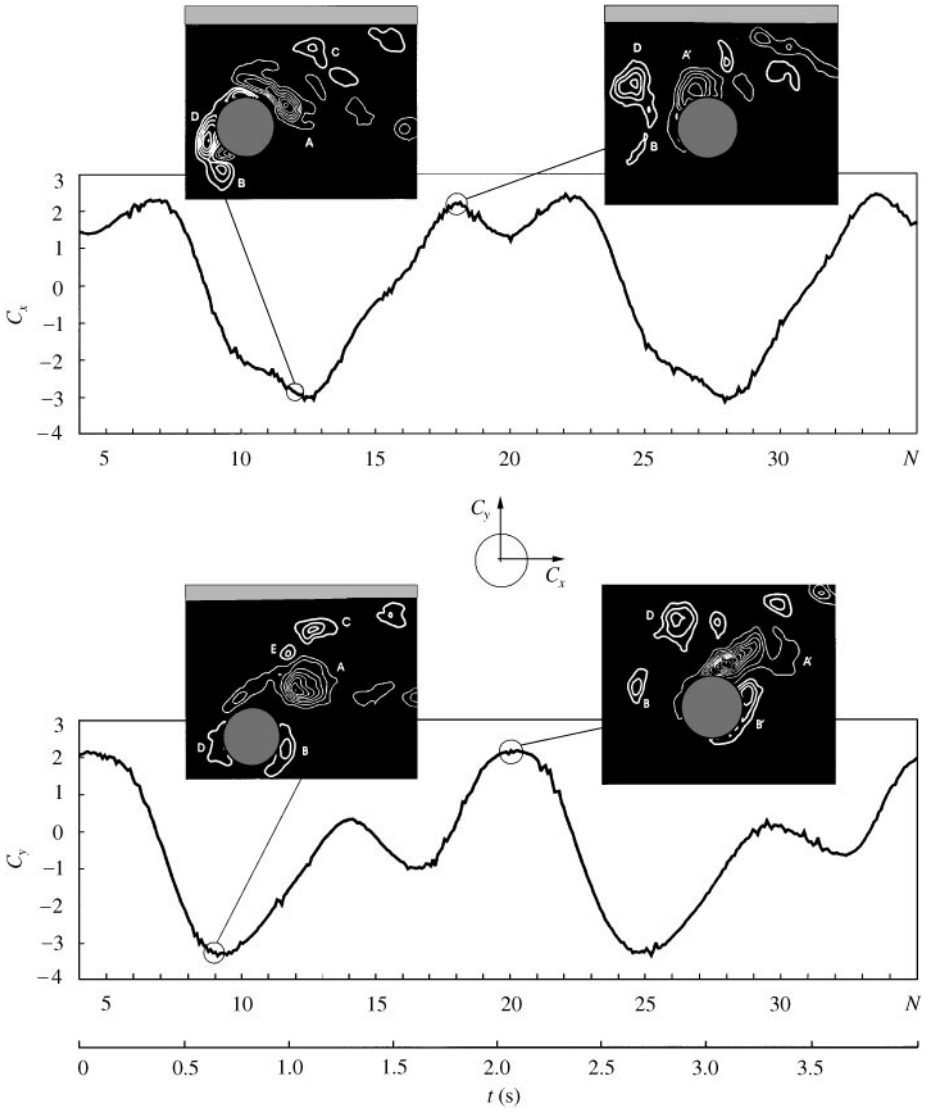

Figure 4. Comparison of selected patterns of instantaneous vorticity with time histories of horizontal C_x and vertical C_y force coefficients for relatively deep submergence of cylinder $h/D = 1{\cdot}57$.

The maximum positive value of C_x, which occurs (initially) at approximately $N = 18$, coincides with the continued development of the large-scale negative vortex A′ along the top surface of the cylinder, as it moves in the clockwise direction above the surface of the cylinder. The remaining concentrations of vorticity, which, of course, contribute to C_x, develop in the fashion described in the previous section.

Concerning the vertical force coefficient C_y, the maximum-negative value coincides with movement of the vorticity concentration A up and away from the surface of the cylinder. On the other hand, the maximum-positive value of C_y occurs when vorticity concentration A′ attains its position at the top of the cylinder during its clockwise migration about the cylinder surface, while the remaining vorticity concentrations develop as previously described.

The relationship between the space–time evolution of the instantaneous velocity field about the cylinder and the effective force **F** acting on the cylinder can be described using a concept described by Wu (1981) and Lighthill (1986). In essence, the vector force acting on a body can be expressed as the time derivative of the spatial integral of the moment of vorticity according to

$$\mathbf{F} = -\frac{\mathrm{d}}{\mathrm{d}t}\left[\rho \int \mathbf{r}\times\boldsymbol{\omega}\,\mathrm{d}V\right], \tag{1a}$$

in which $\boldsymbol{\omega}$ is vorticity, and $\int \mathbf{r}\times\boldsymbol{\omega}\,\mathrm{d}V$ is the integral of moments of vorticity with respect to the center of the body over the entire flow field of volume V. Only the shed vorticity is considered, so forces due to added mass and Froude–Krylov effects are not included in equation (1a). This concept is addressed by Wu (1981) and Unal (1996); additionally, it has been verified by the discrete vortex calculations of Unal (1996). In the case of quasi-two-dimensional flow, the force per unit length on the cylinder can be evaluated from the vorticity field according to the relationship

$$\frac{\mathbf{F}}{l} = -\frac{\mathrm{d}}{\mathrm{d}t}\left[\frac{1}{2}\,\rho \int \mathbf{r}\times\boldsymbol{\omega}\,\mathrm{d}A\right], \tag{1b}$$

in which l is the cylinder length and $\int \mathbf{r}\times\boldsymbol{\omega}\,\mathrm{d}A$ is the integral of the moment of vorticity with respect to the center of the cylinder over the domain of interest, which corresponds to the field of view of the PIV camera. The vorticity is $\boldsymbol{\omega} = \mathbf{k}\omega_z$. Therefore, the horizontal force coefficient can be expressed as $C_x = \mathrm{d}[(M_\omega)_x]/\mathrm{d}t$, where $(M_\omega)_x = -[1/(U^2Dl)]\int y\omega_z\,\mathrm{d}A$ is the normalized integral of the y moment of vorticity that acts in the x direction. Similarly, the vertical force coefficient is $C_y = \mathrm{d}[(M_\omega)_y]/\mathrm{d}t$, where $(M_\omega)_y = -[1/(U^2Dl)]\int x\omega_z\,\mathrm{d}A$ is the normalized integral of the x moment of vorticity.

For the case of deepest nominal submergence of the cylinder, $h/D = 1{\cdot}57$, excerpts of which are shown in Figures 2(a) and 2(b), the free surface remains sufficiently far above the surface of the cylinder, and interactions of vorticity concentrations with the free surface are minimal, thereby providing the opportunity for application of equation (1b). According to equation (1b), the time derivative of the moment of vorticity is required to determine the instantaneous force and, thereby the corresponding force coefficients. Since the temporal resolution of the acquired images is inadequate to allow accurate evaluation of the time derivative, an approach that emphasizes identification of the relative contribution of each of the vorticity concentrations to the induced force coefficients, C_x and C_y, is employed. For the horizontal force coefficient C_x, for example, the time integral of C_x, i.e., $\int C_x\,\mathrm{d}t$, is evaluated from the force transducer data. This measured integral is then compared with the instantaneous moment of vorticity $(M_\omega)_x$. The value of the arbitrary integration constant is chosen in such a way as to match the initial value of $\int C_x\,\mathrm{d}t$ with the initial value of $(M_\omega)_x$. A similar procedure is followed for the vertical force coefficient C_y. This approach was first introduced by Zhu *et al.* (1998).

Figure 5(a) exhibits comparison of: measured $\int C_x\,\mathrm{d}t$, which is designated by the continuous solid line, and moments of vorticity. The top plot of Figure 5(a) emphasizes the separate contributions of the moments $(M_\omega)_x$ corresponding to positive (hollow square symbol) and negative (filled square symbol) vorticity contributions. They exhibit a similar period, but different amplitude and phase shift relative to the measured $\int C_x\,\mathrm{d}t$. The bottom plot of Figure 5(a) focuses on the net moment $(M_\omega)_x$ obtained by summing the positive and negative vorticity contributions to the moment given in the top plot. The variation of the calculated moment generally has the same form as the measured $\int C_x\,\mathrm{d}t$. The discrepancy is no doubt due to a combination of several factors, the most important of which is the

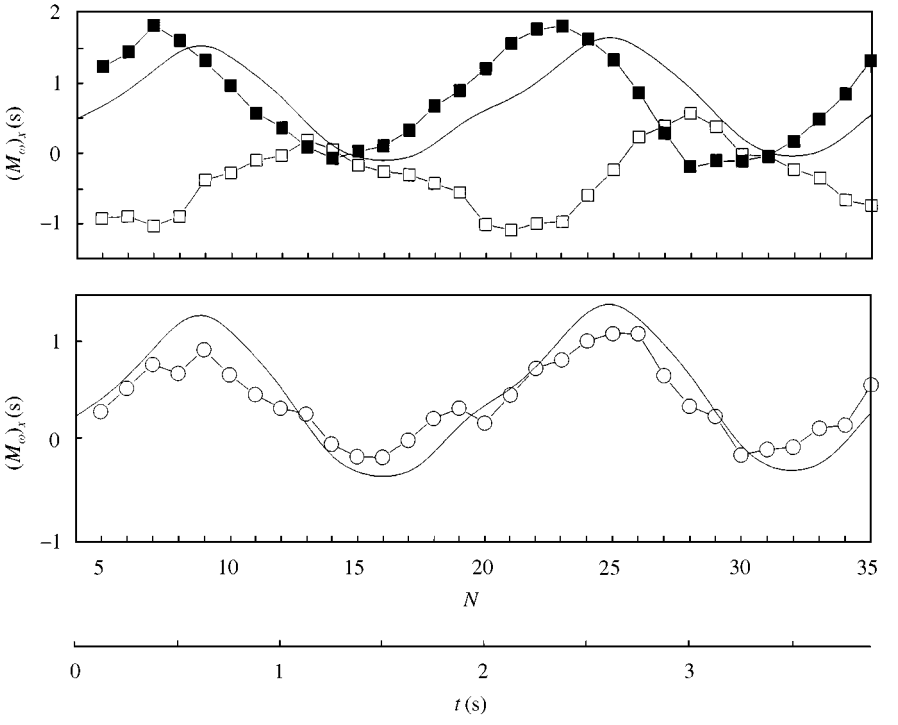

Figure 5(a). Calculated moments of vorticity $(M_\omega)_x$ corresponding to the horizontal (x) direction force: □, contributions from positive vorticity; ■, contribution from negative vorticity concentrations; ○, net sum of positive and negative contributions. Solid line corresponds to the measured time integral of the horizontal force coefficient, $\int C_x \, dt$. Each frame number N corresponds to an instantaneous PIV image. Level of submergence of cylinder is $h/D = 1{\cdot}57$.

existence of low-level vorticity concentrations outside the field of view of the PIV images, excerpts of which are shown in Figures 2(a) and 2(b).

Figure 5(b) provides a similar comparison of the integral of the vertical force coefficient $\int C_y \, dt$ and the calculated moments $(M_\omega)_y$. The top plot again indicates the separate contributions of the moments $(M_\omega)_y$ due to positive and negative vorticity. The overall form of each moment distribution is essentially an inversion of the other, though their amplitudes are different. As a consequence, the variation of the net sum of positive and negative moments, shown in the bottom diagram of Figure 6(b), exhibits small deviations about a nominal value of approximately -1. The lack of agreement between the measured $\int C_y \, dt$ and calculated net moment $(M_\omega)_y$ is most likely due to the failure to account for significant moments arising from large moment arms. Such moments can arise from large values of x, in combination with low level concentrations of vorticity outside the field of view. This situation contrasts with the foregoing case of y moment arms employed to calculate $(M_\omega)_x$, where the value of y is bounded by the presence of the free surface.

5. IDENTIFICATION OF FORCE CONTRIBUTIONS DUE TO INDIVIDUAL VORTICES

Each of the major concentrations of vorticity exhibited in Figures 2(a) and 2(b) will make different contributions to the time integrals of the horizontal and vertical force coefficients, $\int C_x \, dt$ and $\int C_y \, dt$, depending upon the variation of their circulation and position with time

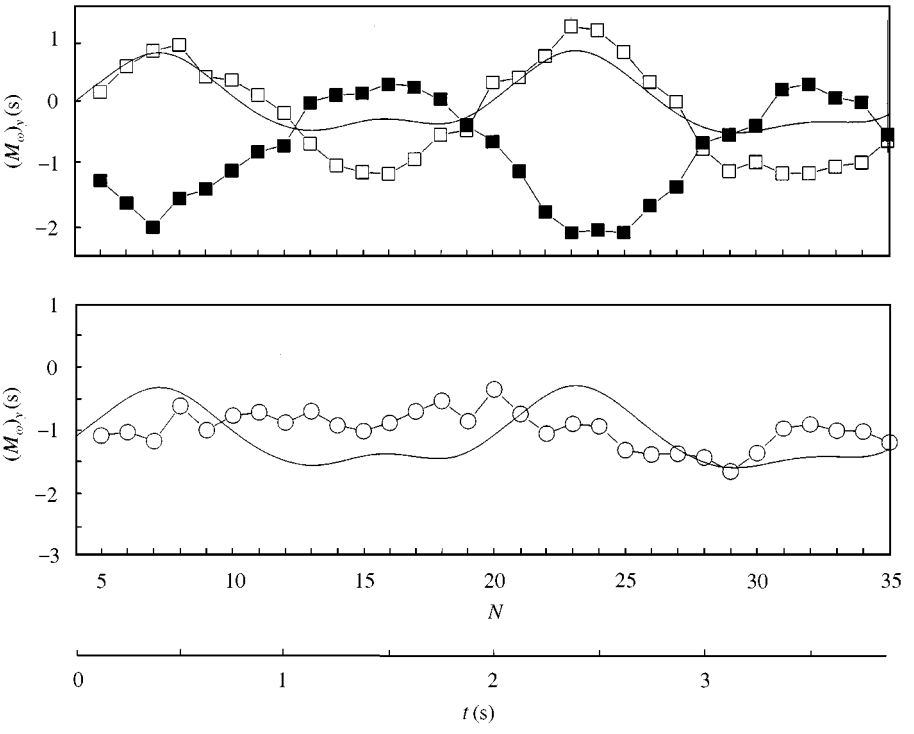

Figure 5(b). Calculated moments of vorticity $(M_\omega)_y$ corresponding to the vertical (y) direction of force □, contributions from positive vorticity concentrations; ■, contribution from negative vorticity concentrations; ○, net sum of positive and negative contributions. Solid line corresponds to the measured time integral of the vertical force coefficient, $\int C_y \, dt$. Each frame number N represents an instantaneous PIV image. Level of submergence of cylinder is $h/D = 1{\cdot}57$.

during the wave cycle. Contributions of the principal vorticity concentrations A, B, C, D, A′, and B′ to the x and y components of the vorticity moments, i.e., $(M_\omega)_x$ and $(M_\omega)_y$, are given in Figure 6.

The top plot of Figure 6 gives the variation of $(M_\omega)_x$ as a function of frame number N. Generally speaking, the major concentrations A and A′ produce the largest moments. Moreover, the change of the vorticity moment with time, represented by the slope $(\Delta(M_\omega)_x/\Delta N)$ has markedly larger values for concentrations A and A′ than those due to the remaining vorticity concentrations B, B′, and C. Comparison with the image sequence of Figures 2(a) and 2(b) shows the physical basis for large changes of the moments due to A and A′. First, consider the rapid movement of vorticity concentration A back towards the cylinder, represented by frames $N = 9$ and 11 in Figure 2; in fact this downward movement continues at least through frame $N = 12$, as shown in the top left image of Figure 4. As a consequence, the values of moment arm y of the vorticity concentration A decrease, producing decreases in the value of $(M_\omega)_x$. This observation is in accord with the pronounced negative value of the slope $(\Delta(M_\omega)_x/\Delta N)$ between frames $N = 9$ and 12 in the upper plot of Figure 6. Moreover, the actual value of the force coefficient C_x shown in Figure 4 attains its largest negative values over $N = 11$ to 13.

On the other hand, movement of vorticity concentration A′ in the upward direction and its continuing increase in scale, evident in frames $N = 17$ and 19 in Figure 2(b), as well as in images $N = 20$ to 23 (not shown herein) promote an increase in the value of the moment arm y and thereby moment $(M_\omega)_x$ of concentration A′ with increasing N; this corresponds to

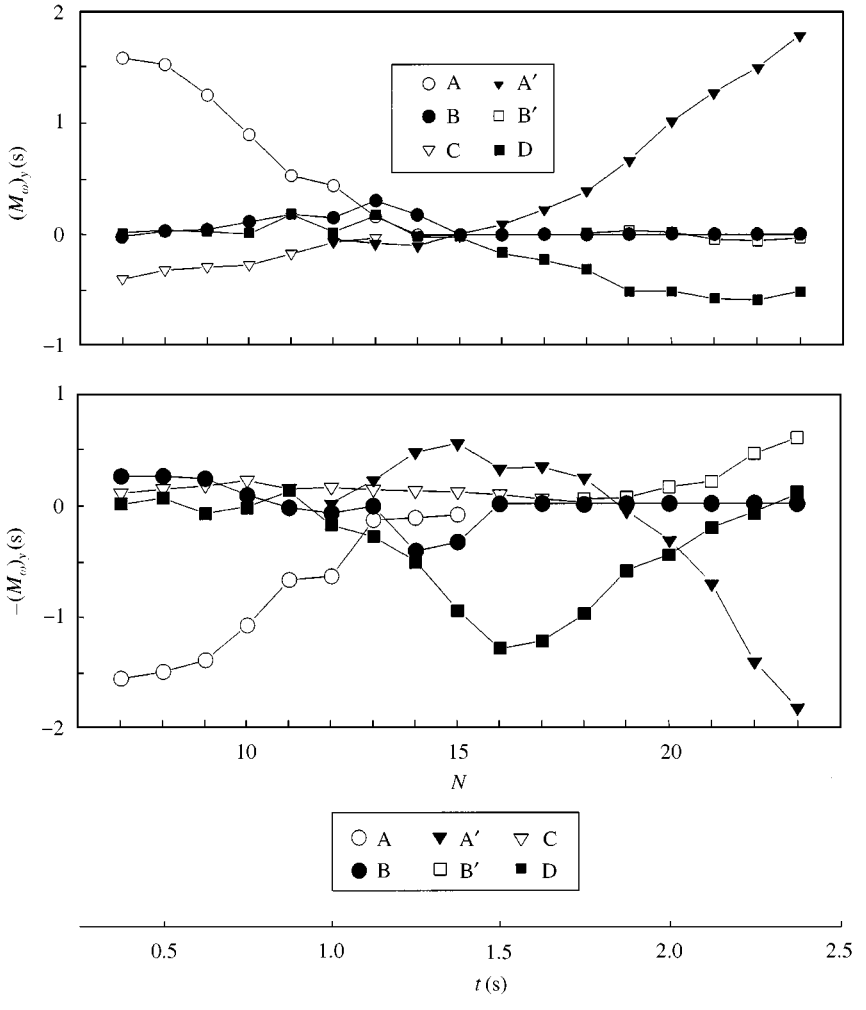

Figure 6. Contributions of major concentrations of vorticity A, B, A′, B′, C and D to the moments of vorticity corresponding to the x and y direction forces. Level of submergence of cylinder beneath the free surface is $h/D = 1{\cdot}57$.

a large positive slope $\Delta(M_\omega)_x/\Delta N$ over $N = 17$ to 23 in Figure 6. In turn, this slope corresponds to the positive peak of C_x over $N = 18$ to 23 in the top trace of Figure 4. To be sure, the concentration of vorticity B,D makes significant, but generally smaller, contributions, as indicated in the top plot of Figure 6.

A similar assessment can be undertaken for the individual contributions to the moment $(M_\omega)_y$ as shown in the bottom plot of Figure 6. The largest contributions to $(M_\omega)_y$ generally are from: concentrations A and A′ over the same portions of the oscillation cycle as for the $(M_\omega)_x$ contributions of the top plot of Figure 6; and concentration B,D during the initial part of its trajectory about the cylinder. The major vorticity concentrations A and A′ produce large positive values of moment $(M_\omega)_y$ at small and large values of N; likewise, concentration B,D yields large moments at intermediate values of N. Again, Figure 2 shows the underlying physics. For vorticity concentration A, frames 7, 9 and 11 suggest decreases in the positive value of $(M_\omega)_y$, due both to a decrease in the peak value of vorticity and a decrease in the x moment arm. This negative slope $\Delta(M_\omega)_y/\Delta N$ produces, in accord with

equation (1), a negative peak in the vertical force coefficient C_y indicated in the bottom plot of Figure 4. Similarly, as indicated in the bottom plot of Figure 6, at large values of $N = 23$ and 24 (not shown), vorticity concentration A′ generates both large positive values of moment $(M_\omega)_y$ and slope of moment $\Delta(M_\omega)_y/\Delta N$, relative to those of the other major vortices B and B′. Correspondingly, the plot of Figure 4 shows the onset of a positive peak of C_y. These observations are due to the movement of the concentration A′ away from the surface of the cylinder; although frames $N = 23$ and 24 are not shown in the image sequence of Figure 2, the initial launching of concentration A′ is evident in frame $N = 19$.

Finally, the bottom plot of Figure 6 also shows that vorticity concentration B,D makes substantial contributions to the moment $(M_\omega)_y$ over the range of intermediate values of N, say $N = 14$ to 19. Attainment of the maximum positive value of moment $(M_\omega)_y$ at $N = 16$ is due to movement of the large-scale concentration B,D to the left of the cylinder, as shown in Figure 2(b). At this instant, the slope of the moment $\Delta(M_\omega)_y/\Delta N$ is approximately zero, and the value of C_y in Figure 4 is small, i.e., slightly positive.

On the basis of the foregoing observations of the dominant contributions of negative vortices A, A′ and the positive vortex B,D to both $(M_\omega)_x$ and $(M_\omega)_y$, we conclude that such contributions occur in the relatively early stages of development of these vorticity concentrations, corresponding to small displacements away from the surface of the cylinder. This effect, involving a relatively short moment arm and large circulation of the vorticity concentration, appears to be more prevalent than the large moment arm and reduced value of circulation of the vorticity concentrations associated with large orbital trajectories.

6. EFFECTS OF DEGREE OF SUBMERGENCE OF CYLINDER: SPACE–TIME EVOLUTION OF VORTICITY PATTERNS

Figure 7 shows a time sequence of images of the instantaneous vorticity distribution for three depths of nominal submergence of the cylinder: relatively deep submergence ($h/D = 1{\cdot}57$), corresponding to the first row of images; intermediate submergence ($h/D = 0{\cdot}55$), shown in the second row; and surface-piercing ($h/D = 0$), given in the third row of images. Each time sequence consists of representative images over the span of frame numbers $N = 7$ through 19. At a given value of N, the phase of the undulating free surface relative to the cylinder is the same.

6.1. Initial Stage of Development of Patterns of Vorticity

In the layout of Figure 7(a), corresponding to frames $N = 7$ and 9, analogous concentrations of vorticity A, B and C are identifiable for all levels of submergence h/D. Their form, circulation and position, however, vary substantially. At the deepest submergence (top row of images), vorticity concentration A takes an approximately circular form, whereas at the intermediate depth of submergence (middle row), concentration A is substantially elongated and eventually takes the form of a sequence of small-scale concentrations of vorticity embedded in a vorticity layer. For the shallowest submergence (bottom row), corresponding to surface piercing during a subsequent instant of the wave cycle, vorticity concentration A is dramatically reduced in both the circulation and spatial extent. It initially appears on the upper surface of the cylinder, then migrates in the clockwise direction and, in conjunction with interaction of vorticity concentration B with the cylinder, it eventually takes the form of two distinct vorticity concentrations. Taking an overview of the evolution of vorticity concentration B for varying degrees of submergence, its peak level of vorticity increases with decreasing h/D; at the shallowest submergence, i.e., smallest value of h/D, it

takes on a highly concentrated form. Finally, vorticity concentration C appears above the cylinder at the deep and intermediate values of submergence, but is located adjacent to the lower surface of the cylinder at the shallowest submergence. Generally speaking, the effect of decreasing submergence is to retard the orbital motion of vorticity concentration C in the clockwise direction.

6.2. Intermediate Stage of Development of Patterns of Vorticity

The next sequence of events is represented in Figure 7(b) by frames $N = 11$ and 15. For deep submergence (top row), vorticity concentration A is on the return part of its trajectory, about to collide with the cylinder at $N = 11$, and only a small residual of the post-collision process is evident at $N = 15$. On the other hand, the major vortex A at intermediate submergence (middle row) does not directly encounter the cylinder and remains intact at $N = 15$. At the shallowest submergence (bottom row), generation of vortex A is retarded relative to deeper values of submergence, and it occurs from the bottom surface of the cylinder at $N = 11$. At $N = 15$, the separated vortex A is located well away from the surface of the cylinder. At all levels of submergence, for the images at $N = 15$, an additional concentration of vorticity A′ is generated from the left side of the cylinder; it is the sequel to the originally generated vortex A from an earlier portion of the wave cycle. The degree of concentration of vorticity A′ appears to increase with decreasing submergence.

Moreover, all levels of submergence of the cylinder exhibit formation of vorticity concentrations B and D. The sequence of events leading to their initial development at $N = 11$, as well as their subsequent evolution at $N = 15$, is similar for deep (top row) and intermediate (middle row) values of submergence. At shallow submergence (bottom row of images), however, vortex B separates early from the surface of the cylinder, and at $N = 11$, appears immediately beneath extended vorticity concentration A. At a later time, $N = 15$, concentration B moves well to the left of the cylinder.

Further, vorticity concentration C continues its orbital trajectory about the cylinder at deep submergence in images $N = 11$ and 15, collides with the free surface at $N = 1$ for intermediate submergence, and remains well submerged beneath the free surface at the shallowest submergence, both in images $N = 11$ and 15.

A distinctive feature of the vorticity field development at the shallowest submergence of the cylinder is generation of an additional concentration of vorticity E from the free surface at $N = 15$. It is induced by vortex *D*. All of these events at the shallowest submergence produce two sets of triplet vortices at $N = 15$; together, they form an array of six counter-rotating vortices.

6.3. Final Stage of Development of Patterns of Vorticity

The final stage of development is indicated in Figure 7(c). At relatively deep submergence (top row of images), vortices A′, B and D migrate in the clockwise direction in accord with the wave trajectory, and vortex B′ appears on the lower surface of the cylinder at $N = 19$.

For intermediate submergence (middle row), vorticity concentration A, which, unlike the case of deepest submergence, did not collide with the cylinder, is still identifiable. Development of concentration A′ in images $N = 17$ and 19 is closely similar to its development at the deepest submergence. Vorticity pattern B,D retains its identity of two concentrations at $N = 17$; they appear distinctly separated at $N = 19$.

At the shallowest submergence, the array of six counter-rotating concentrations of vorticity is still identifiable at $N = 17$, though the peak vorticity levels of each of the

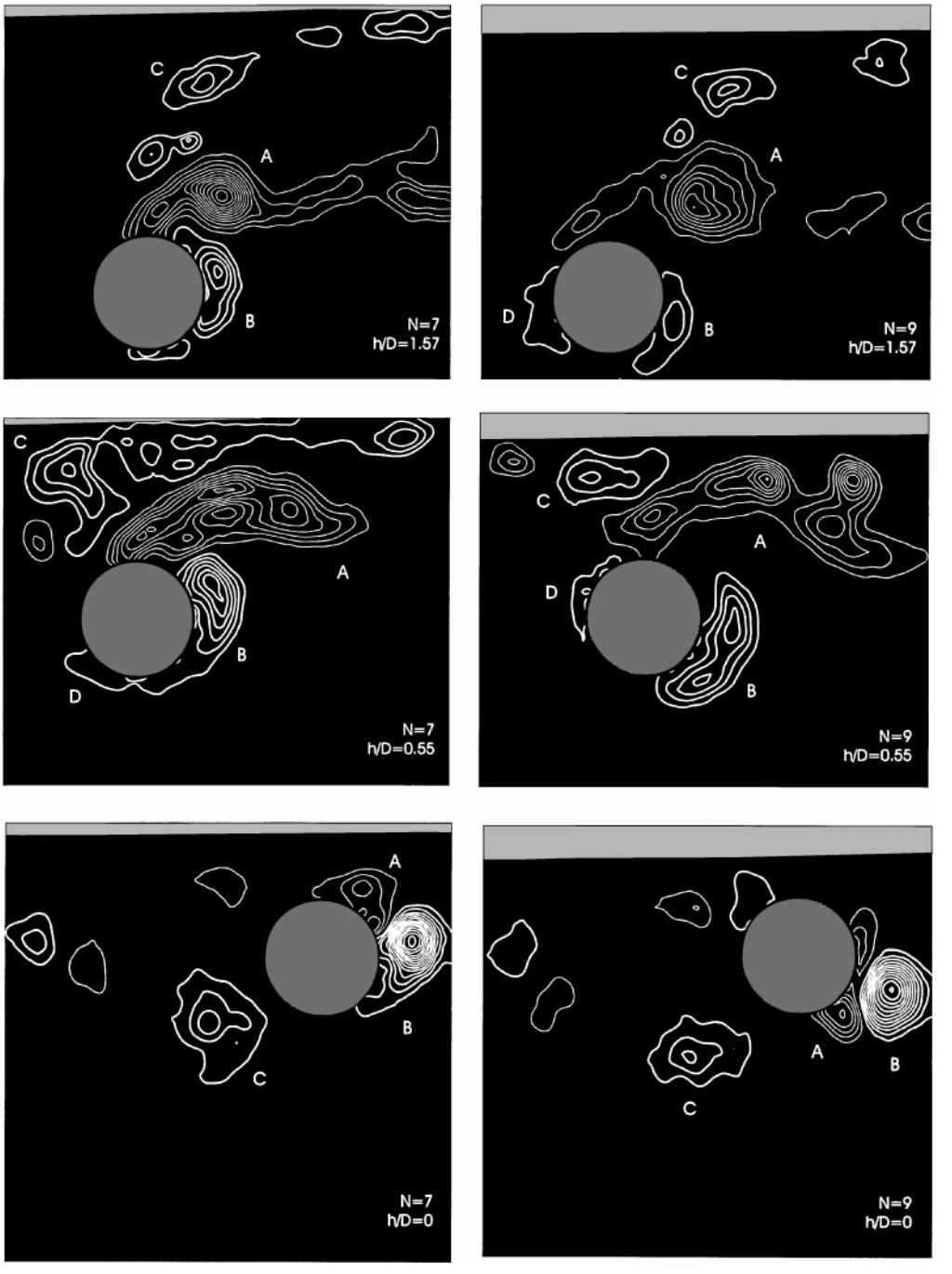

Figure 7(a). Comparison of instantaneous patterns of vorticity at the same frame numbers $N = 7$ and 9 for varying levels of submergence $h/D = 1{\cdot}57$, 0·55, and 0 of the cylinder beneath the free surface. Frame $N = 7$ represents the instant where the crest of the free surface wave is above the cylinder. Minimum and incremental values of vorticity are $\omega_{\min} = 3\,\mathrm{s}^{-1}$ and $\Delta\omega = 3\,\mathrm{s}^{-1}$.

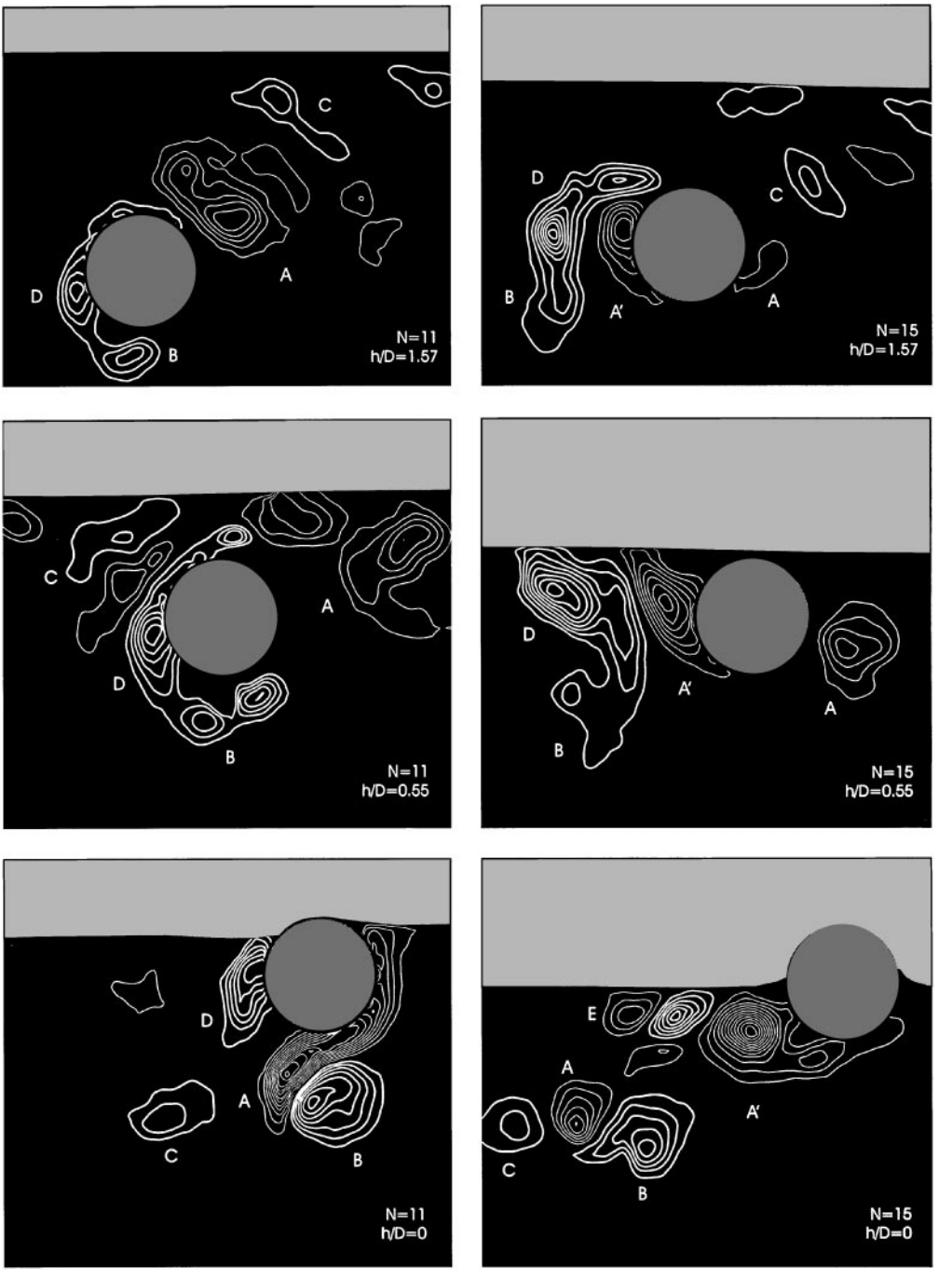

Figure 7(b). Comparison of instantaneous patterns of vorticity at the same frame numbers $N = 11$ and 15 for varying levels of submergence $h/D = 1{\cdot}57$, $0{\cdot}55$, and 0 of the cylinder beneath the free surface. Frame $N = 15$ represents the instant at which the trough of the free surface wave is above the cylinder. Minimum and incremental values of vorticity are $\omega_{\min} = 3\ \mathrm{s}^{-1}$ and $\Delta\omega = 3\ \mathrm{s}^{-1}$.

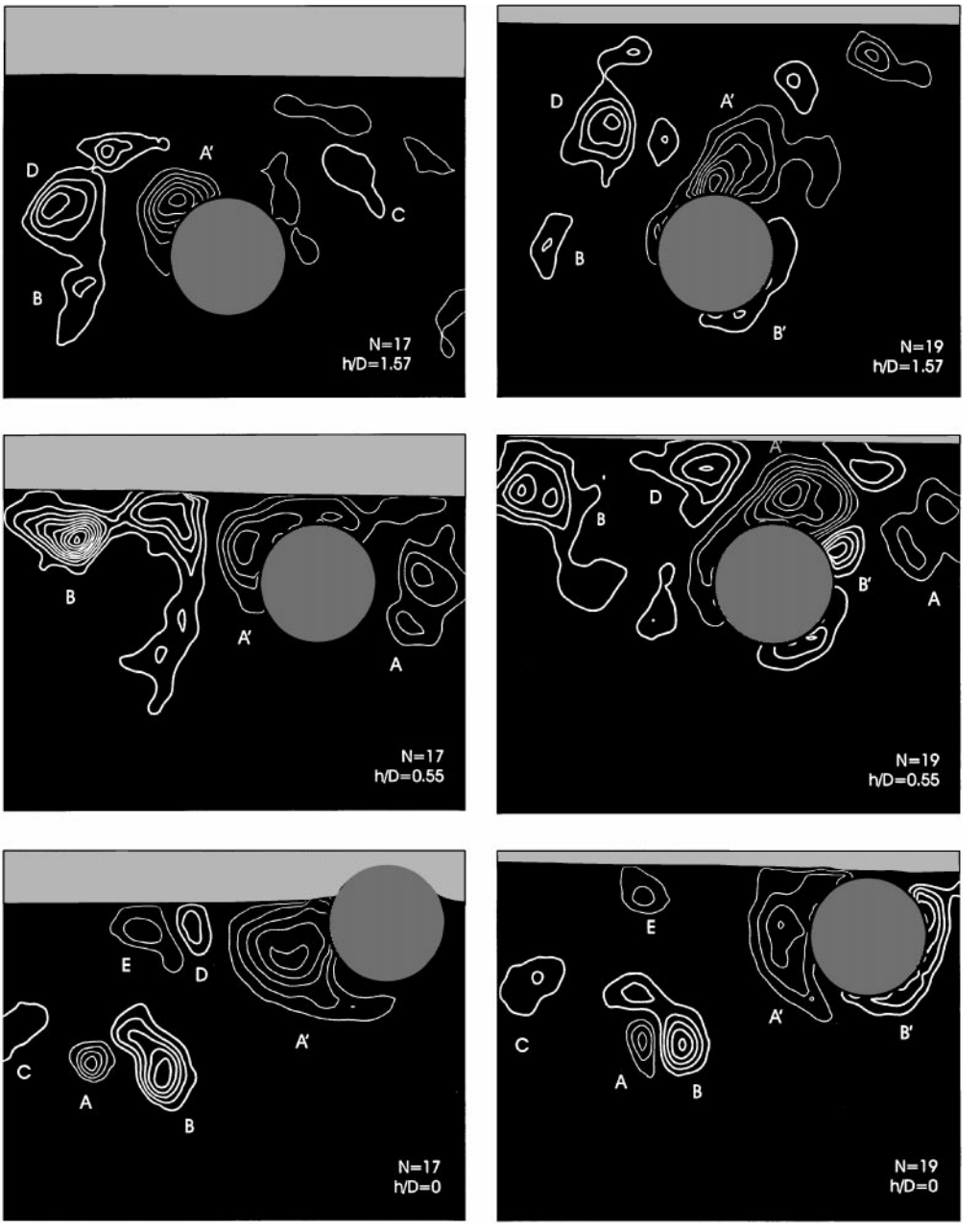

Figure 7(c). Comparison of instantaneous patterns of vorticity at the same frame numbers $N = 17$ and 19 for varying levels of submergence $h/D = 1{\cdot}57$, $0{\cdot}55$, and 0 of the cylinder beneath the free surface. Minimum and incremental values of vorticity are $\omega_{\min} = 3\,\mathrm{s}^{-1}$ and $\Delta\omega = 3\,\mathrm{s}^{-1}$.

concentrations has generally decreased. At $N = 19$, onset of vorticity concentration B′ along the right surface of the cylinder occurs in a fashion analogous to that at intermediate and deep levels of submergence.

7. CONCLUDING REMARKS

Interaction of a free surface wave with a horizontal cylinder is examined at a sufficiently high value of Keulegan–Carpenter number such that well-defined concentrations of vorticity are generated during a typical wave cycle. The mutual interaction of these vorticity concentrations at varying degrees of submergence beneath the free surface provides a rich array of space–time patterns of the instantaneous vorticity field. Irrespective of the particular pattern, however, central elements of the vortex formation process appear to persist. In essence, due to orbital motion of the wave, the evolution of a given pattern of vorticity follows a well-defined sequence: (i) growth of a pronounced region of vorticity having an identifiable extremum on the surface of the cylinder; (ii) migration of this vorticity concentration about the surface of the cylinder in a direction compatible with the orbital motion of the wave; and (iii) separation of the vorticity concentration from the surface of the cylinder. This process of growth and migration of a vorticity concentration can originate from three sites, i.e., approximately on the upper, right, and lower surfaces of the cylinder, during a single oscillation cycle.

The foregoing process appears to be largely controlled by the orbital motion of the wave. In fact, the form and orientation of the orbital trajectories of the eventually formed concentrations of vorticity resemble those of the particle trajectories of the wave. Basically, two types of orbits of the vorticity concentrations are discernible. The first is a relatively small-amplitude orbit; in the limiting case of such an orbit, abrupt reversal in direction of movement of the vorticity concentration occurs, followed by collision of the concentration with the surface of the cylinder for sufficiently deep submergence. This type of small-amplitude orbital motion is shown to actually give rise to relatively large moments of vorticity and large contributions to the instantaneous forces on the cylinder, as deduced by application of a concept described by Lighthill (1986). The second type of orbital motion of the vorticity concentrations exhibits a large-amplitude trajectory. At a sufficiently large value of nominal submergence, the vorticity concentration navigates one complete loop about the cylinder. This type of large-amplitude orbit, however, generally gives rise to smaller moments of vorticity. This is due to the fact that the large-amplitude orbit involves a relatively long time scale, and thereby the opportunity for substantial decay of circulation of the vortex.

The nominal submergence of the cylinder beneath the wave has a pronounced effect on the pattern of vorticity concentrations. It has been demonstrated that generic concentrations of vorticity are common to all patterns of vorticity at various depths of submergence. For relatively deep submergence, as previously noted, the separated vorticity concentrations exhibit large-scale orbital motion about the cylinder. For intermediate submergence, however, the presence of the free surface exerts a significant influence, and this large-scale orbital motion is substantially hindered. Moreover, the distorted velocity field of the wave, due to proximity of the free surface of the cylinder, promotes formation of elongated vorticity concentrations from the top of the cylinder and, in addition, significantly enhances the vorticity level and scale of the vorticity concentrations from the bottom surface of the cylinder. In the extreme case of shallow submergence, whereby the cylinder pierces the free surface during the wave cycle, the presence of the free surface induces a substantial lag of the process of vortex formation from the surface of the cylinder. In addition, vortex formation is induced from the free surface during a portion of the wave cycle. These

fascinating processes of vortex formation and interaction yield an ordered array of as many as six counter-rotating vortices immediately beneath the free surface.

Finally, it has been demonstrated that, at relatively large submergence, the space–time evolution of the vorticity field is associated with identifiable topological features of the instantaneous streamline patterns. Changes in the predominant orientation of the velocity field of the undisturbed portion of the free-surface wave, in conjunction with the defined patterns of positive and negative vorticity concentrations about the cylinder, can induce well-defined singularities in the form of foci and saddle points. Even though the pattern of vorticity concentrations undergoes a very mild change from one instant to the next during the wave motion, nearly discontinuous changes in the streamline topology can occur. Such changes include, for example, abrupt switching of the location of a saddle point from one region of the flow to another. These changes are apparently due to the fact that the predominant direction of the velocity field of the wave varies substantially during the wave cycle.

ACKNOWLEDGMENTS

The authors gratefully acknowledge the primary financial support of the Office of Naval Research under Grants N00014-94-1-1183 and N00014-94-1-0815, P00001, monitored by Dr Thomas Swean. Supplemental support was provided by the National Science Foundation under Grant CTS-9803734, monitored by Dr John Foss. Moreover, the authors are indebted to extensive discussions with and a lecture series by Professor M. F. Unal of Istanbul Technical University during a stay at Lehigh University funded by a Fulbright grant.

References

Anagnostopoulos, P., Iliadis, G. & Ganoulis, J. 1995 Flow and response parameters of a circular cylinder vibrating in-line with an oscillating stream. In *Flow-Induced Vibration* (ed. P. W. Bearman), pp. 167–179. Rotterdam: Balkema.

Baba, N. & Miyata, H. 1987 Higher-order accurate difference solutions of vortex generation from a circular cylinder in an oscillatory flow. *Journal of Computational Physics* **69,** 362–396.

Bearman, P. W., Chaplin, J. R., Graham, J. M. R., Kostense, J. K., Hall, P. F. & Klopman, G. 1985b The loading on the cylinder in post-critical flow beneath periodic and random waves. In *Proceedings of 4th Conference on Behaviour of Offshore Structures*, Vol. 2, pp. 213–225: Netherlands: Delft.

Bearman, P. W., Downie, M. J., Graham, J. M. R. & Obasaju, F. D. 1985a Forces on cylinders in viscous oscillatory flow at low Keulegan–Carpenter numbers. *Journal of Fluid Mechanics* **154,** 337–356.

Bearman, P. W., Graham, J. M. R., Naylor, P. & Obasaju, E. D. 1981 The role of vortices in oscillatory flow about bluff bodies. In *Proceedings of International Symposium on Hydrodynamics and Ocean Engineering*, pp. 621–644. Trondheim: The Norwegian Institute of Technology.

Borthwick, A. 1986 Orbital flow past a cylinder: a numerical approach. *International Journal for Numerical Methods in Fluids* **6,** 677–713.

Borthwick, A. 1987 Orbital flow past a cylinder: experimental work. In *Proceedings of the 5th Conference of Offshore Mechanics and Arctic Engineering*, p. 123.

Chaplin, J. R. 1981a On the irrotational flow around a horizontal cylinder in waves. *Journal of Applied Mechanics* **48,** 689–694.

Chaplin, J. R. 1981b Boundary layer separation from a cylinder in waves. In *Proceedings of International Symposium on Hydrodynamics in Ocean Engineering*, Vol. 1, pp. 645–666. Trondheim, Norway.

Chaplin, J. R. 1984 Nonlinear forces on a horizontal cylinder beneath waves. *Journal of Fluid Mechanics* **147,** 449–464.

CHAPLIN, J. R. 1988 Loading on a cylinder in oscillatory flow: elliptical orbital flow. *Applied Ocean Research* **10,** 199–206.

CHAPLIN, J. R. 1992 Orbital flow around a circular cylinder. Part 1. Steady streaming in non-uniform conditions. *Journal of Fluid Mechanics* **237,** 395–411.

CHAPLIN, J. R. 1993 Orbital flow around a circular cylinder. Part 2. Attached flow at larger amplitudes. *Journal of Fluid Mechanics* **246,** 397–418.

GRASS, A. J., SIMONS, R. R. & CAVANAUGH, N. J. 1985 Fluid loading on horizontal cylinders in wave type orbital flow. In *Proceedings of 4th Conference of Offshore Mechanics an Arctic Engineering*, Vol. 1, pp. 576–583, Dallas, TX.

HOLMES, P. & CHAPLIN, J. R. 1978 Wave loads on horizontal cylinders. In *Proceedings of 16th International Conference on Coastal Engineering*, Vol. 3, pp. 2449–2460, Hamburg.

HONJI, H. 1981 Streaked flow around an oscillating circular cylinder. *Journal of Fluid Mechanics* **107,** 509–520.

IKEDA, S. & YAMAMOTO, Y. 1981 Lift force on cylinders in oscillatory flows. In *Report of Department of Foundation Engineering and Construction Engineering*, pp. 1–16, Saitama University, Japan.

IWAGAKI, Y., ASANO, T. & NAGAI, F. 1983 Hydrodynamic forces on a circular cylinder placed in wave-current co-existing fields. In *Memo Faculty of Engineering*, Vol. 45, pp. 11–23, Japan: Kyoto University.

JUSTESEN, P. 1991 A numerical study of oscillating flow around a circular cylinder. *Journal of Fluid Mechanics* **222,** 157–196.

LIGHTHILL, J. 1986 Fundamentals concerning wave loading on offshore structures. *Journal of Fluid Mechanics* **173,** 667–681.

LIN, X. W., BEARMAN, P. W. & GRAHAM, J. M. R. 1996 A numerical study of oscillatory flow about a circular cylinder for low values of beta parameter. *Journal of Fluids and Structures* **10,** 501–526.

LIN, J.-C. & ROCKWELL, D. 1996 Force identification by vorticity fields: techniques based on flow imaging. *Journal of Fluids and Structures* **10,** 663–668.

LIN, J.-C. & ROCKWELL, D. Horizontal oscillations of a cylinder beneath a free surface: vortex formation and loading. *Journal of Fluid Mechanics* (submitted).

LIN, J.-C., SHERIDAN, J. & ROCKWELL, D. 1996 Near-wake of a perturbed, horizontal cylinder at a free-surface. *Physics of Fluids* **8,** 2107–2116.

MAULL, D. J. & MILLINER, M. G. 1978 Sinusoidal flow past a circular cylinder. *Coastal Engineering* **2,** 149–168.

MIYATA, H. & LEE, Y.-G. 1990 Vortex motions about a horizontal cylinder in waves. *Ocean Engineering* **17,** 279–305.

MIYATA, H., SHIKAZONO, N. & KANAI, M. 1990 Forces on a circular cylinder advancing steadily beneath the free surface. *Ocean Engineering* **17,** 81–104.

NAUDASCHER, E. & ROCKWELL, D. 1994 *Flow-Induced Vibrations*: *An Engineering Guide*. Rotterdam: Balkema Press.

NOCA, F. 1997 On the evaluation of time-dependent fluid dynamic forces on bluff bodies. Ph.D. Dissertation, California Institute of Technology, Pasadena, California, U.S.A.

NOCA, F., SHIELS, D. & JEON, D. 1997 Measuring instantaneous fluid dynamic forces on bodies, using only velocity field and their derivatives. *Journal of Fluids and Structures* **11,** 345–350.

OBASAJU, E. D., BEARMAN, P. W. & GRAHAM, J. M. R. 1988 A study of forces, circulation and vortex patterns around a circular cylinder in oscillating flow. *Journal of Fluid Mechanics* **196,** 467–494.

RAMBERG, S. E. & NIEDZWECKI, J. M. 1979 Some uncertainties and errors in wave force computations. In *Proceedings of 11th Offshore Technology Conference*, Vol. 3, pp. 2091–2101. Houston, TX, U.S.A.

ROCKWELL, D., MAGNESS, C., TOWFIGHI, J., AKIN, O. & CORCORAN, T. 1993 High image-density particle image velocimetry using laser scanning techniques. *Experiments in Fluids* **14,** 181–192.

SARPKAYA, T. 1963 Lift, drag, and added-mass coefficients for a circular cylinder immersed in a time-dependent flow. *Journal of Applied Mechanics* **85,** 13–15.

SARPKAYA, T. 1968 An analytical study of separated flow about circular cylinders. *ASME Journal of Basic Engineering* **90,** 511–520.

SARPKAYA, T. 1969 Analytical study of separated flow about circular cylinders. *Physics of Fluids* **12,** Supplement II, 145.

SARPKAYA, T. 1977 In-line and transverse forces on cylinders in oscillatory flow at high Reynolds numbers. *ASCE Journal of Ship Research* **21,** 200–216.

SARPKAYA, T. 1984 Discussion of paper by Stansby, P. K. *et al*., Quasi 2D forces on a vertical cylinder in waves. *ASCE Journal of Waterway*, *Port*, *Coastal and Ocean Engineering* **110,** 120–124.

Sarpkaya, T. 1986 Force on a circular cylinder in viscous oscillatory flow at low keulegan-carpenter numbers. *Journal of Fluid Mechanics* **165,** 61–71.
Sarpkaya, T. 1989 Computation methods with vortices—the 1988 Freeman scholar lecture. *ASME Journal of Fluids Engineering* **111,** 5–52.
Sarpkaya, T. & Isaacson, M. 1981 *Mechanics of Wave Forces on Offshore Structures*. New York: Van Nostrand Reinhold.
Sheridan, J., Lin, J.-C. & Rockwell, D. 1997 Flow past a cylinder close to a free surface. *Journal of Fluid Mechanics* **330,** 1–30.
Singh, S. 1979 Forces on bodies in oscillatory flow. Ph.D. Thesis, University of London, London, England.
Sun, X. & Dalton, C. 1996 Application of the LES method to the oscillating flow past a circular cylinder. *Journal of Fluids and Structures* **10,** 851–872.
Tatsuno, M. & Bearman, P. W. 1990 A visual study of the flow around an oscillating circular cylinder at low Keulegan–Carpenter numbers and low stokes numbers. *Journal of Fluid Mechanics* **211,** 157–182.
Unal, M. F. 1996 Force calculation by control volume and vortex methods. Lecture Series, Department of Mechanical Engineering and Mechanics, Lehigh University, Bethlehem, Pennsylvania, U.S.A.
Unal, M. F., Lin, J.-C. & Rockwell, D. 1997 Force prediction via PIV: a momentum-based approach. *Journal of Fluids and Structures* **11,** 965–971.
Van Dyke, M. 1982 *An Album of Fluid Motion*, p. 110. Stanford: Parabolic Press.
Wang, X. & Dalton, C. 1991 Oscillating flow past a rigid circular cylinder: a finite difference calculation. *ASME Journal of Fluids Engineering* **13,** 377–383.
Williamson, C. H. K. 1985 Sinusoidal flow relative to circular cylinders. *Journal of Fluid Mechanics* **155,** 141–174.
Williamson, C. H. K., Hess, P., Peter, M. & Govardhan, R. 1998 Fluid loading and vortex dynamics for a body in elliptic orbits. *Proceedings of 1998 ASME Fluids Engineering Division Summer Meeting*, Washington, DC.
Wu, J. C. 1981 Theory for aerodynamic force in viscous flows. *AIAA Journal* **19,** 432–441.
Zhu, Q., Lin, J.-C., Unal, M. F. & Rockwell, D. 1998 Motion of a cylinder adjacent to a free surface: flow patterns and loading. *Experiments in Fluids* (submitted).